

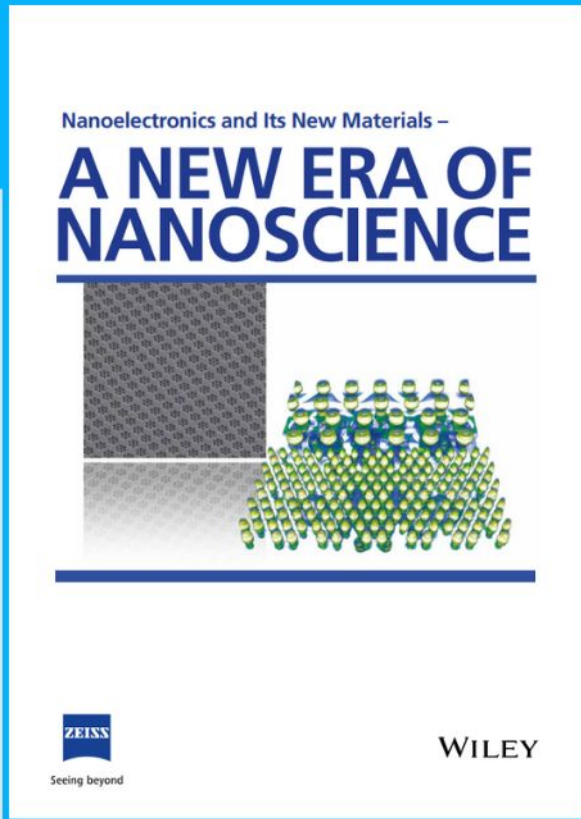


Nanoelectronics and Its New Materials – A NEW ERA OF NANOSCIENCE

Discover the recent advances in electronics research and fundamental nanoscience.

Nanotechnology has become the driving force behind breakthroughs in engineering, materials science, physics, chemistry, and biological sciences. In this compendium, we delve into a wide range of novel applications that highlight recent advances in electronics research and fundamental nanoscience. From surface analysis and defect detection to tailored optical functionality and transparent nanowire electrodes, this eBook covers key topics that will revolutionize the future of electronics.

To get your hands on this valuable resource and unleash the power of nanotechnology, simply download the eBook now. Stay ahead of the curve and embrace the future of electronics with nanoscience as your guide.



Seeing beyond

WILEY

Thermal Emission Manipulation Enabled by Nano-Kirigami Structures

Yinghao Zhao, Qinghua Liang, Sufan Li, Yingying Chen, Xing Liu, Haozhe Sun, Chong Wang, Chang-Yin Ji, Jiafang Li,* and Yang Wang*

The nano-kirigami metasurfaces have controllable 3D geometric parameters and dynamic transformation functions and therefore provide a strong spectral regulation capability of thermal emission. Here, the authors propose and demonstrate a dynamic and multifunctional thermal emitter based on deformable nano-kirigami structures, which can be actuated by electronic bias or mechanical compression. Selective emittance and the variation of radiation intensity/wavelength are achieved by adjusting the geometric shape and the transformation of the structures. Particularly, a thermal management device based on a composite structure of nano-kirigami and polydimethylsiloxane (PDMS) thin film is developed, which can dynamically switch the state of cooling and heating by simply pressing the device. The proposed thermal emitter designs with strong regulation capability and multiple dynamic adjustment strategies are desirable for energy and sensing applications and inspire further development of infrared emitters.

control of external stimuli such as electric voltage,^[13] temperature change,^[14–17] mechanical strain,^[18] and so on.^[19–21] However, most of the systems shown to date have limited control capability that can only adjust either the radiation intensity or the peak wavelength in a certain mode, and the method of dynamic control is limited. A thermal emission manipulation platform with multi-dimensional regulation capability is desired for modern optical systems with different applications.

Among many metasurface designs, nano-kirigami structures with unique driving modes are promising candidates for thermal emission manipulation, as their optical properties can be controlled by geometrical parameters and structural transformation. Versatile optical responses of nano-kirigami structures have been

demonstrated in both visible and near-infrared wavelengths, including Fano resonance,^[22] chiral inversion,^[23] phase regulation,^[24] circular dichroism reversal,^[25] and so on. Through a facile nanofabrication process, various 2D and 3D kirigami structures can be realized on metal or dielectric films. Moreover, the deformable structures of nano-kirigami can be actuated by employing external stimuli such as electronic bias,^[26] mechanical compression,^[22] and pneumatic pressure,^[27] making them a realistic solution for dynamic thermal control applications. Nevertheless, nano-kirigami structures with large pixel sizes for mid-infrared wavelengths remain unexplored.

Here, a new way of regulating thermal emission is explored based on the nano-kirigami structures. The selective emittance is readily achieved by adjusting the geometric shape of nano-kirigami structures. The structures are reversibly transformed from 2D to 3D by electromechanical reconfiguration, resulting in changes in emittance while nearly unchanging the peak emission wavelength. We further demonstrate a thermal management device based on a composite structure of nano-kirigami and polydimethylsiloxane (PDMS) thin film, which can be dynamically switched from a solar absorber to a radiative cooling emitter by simply pressing the device. The proposed thermal emission control method with strong spectral regulation capability and multiple dynamic adjustment strategies are desirable for energy and sensing applications and could inspire further development of infrared emitters.

1. Introduction

Regulating the thermal emission of objects has many important applications such as temperature management,^[1] energy utilization,^[2–4] solar thermophotovoltaic,^[5–7] thermal information processing,^[8] and thermal camouflage.^[9] The thermal emission of natural objects is mostly incoherent light that is broadband, non-polarized, and angular independent. And changing the temperature is the main method to dynamically regulate the thermal emission power.^[10–12] With the development of nanotechnology in recent decades, metasurface generates many novel electromagnetic behaviors through the interaction between wavelength size structure and light and provides more freedom for regulating thermal emission. In addition to temperature modulation, time-dependent emittance can be achieved by instant

Y. Zhao, Q. Liang, S. Li, Y. Chen, X. Liu, H. Sun, C. Wang, C.-Y. Ji, J. Li, Y. Wang
Key Lab of Advanced Optoelectronic Quantum Architecture and Measurement (Ministry of Education)
Beijing Key Lab of Nanophotonics & Ultrafine Optoelectronic Systems and School of Physics
Beijing Institute of Technology
Beijing 100081, China
E-mail: jiafangli@bit.edu.cn; yangwang@bit.edu.cn

The ORCID identification number(s) for the author(s) of this article can be found under <https://doi.org/10.1002/sml.202305171>

DOI: 10.1002/sml.202305171

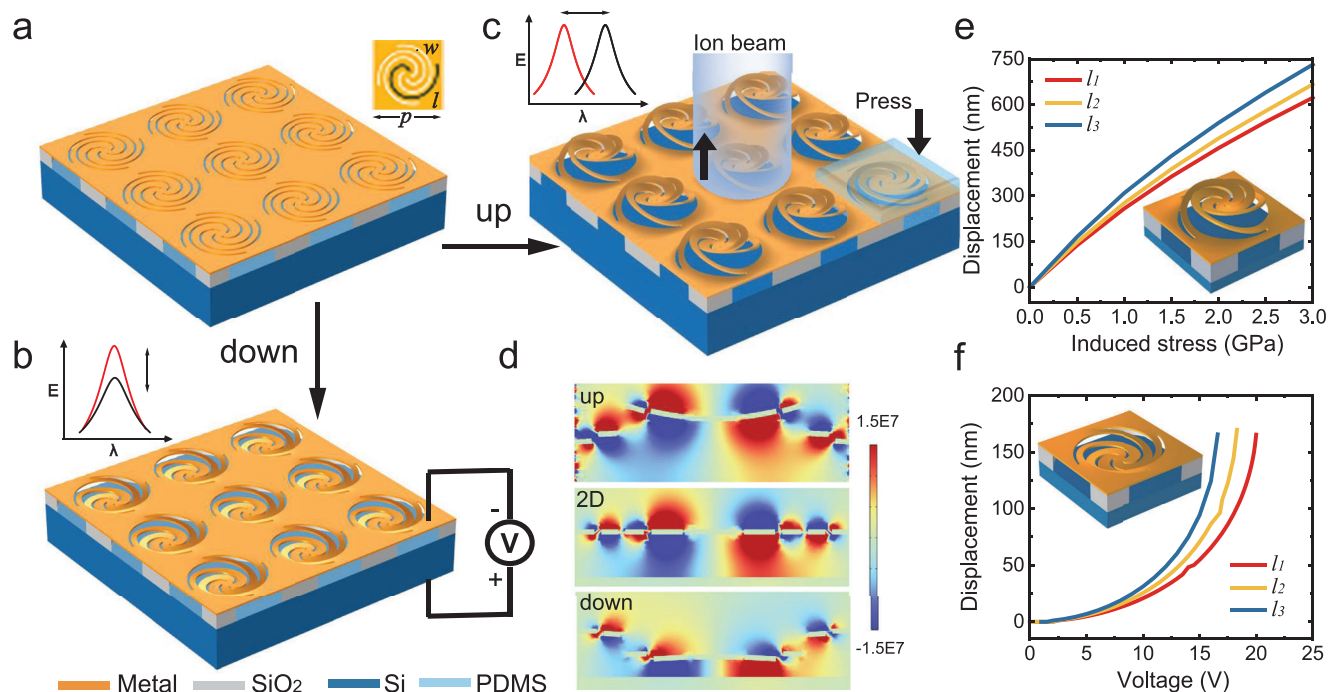


Figure 1. Schematic of the designed nano-kirigami structures and the dynamic driving methods. a) Schematic of a 2D nano-kirigami array and b) its downward 3D state and c) its upward 3D state. d) Normalized E_z distributions in xz plane at the plasmonic resonance wavelength. The mirror symmetry of the field distribution with respect to the xy plane is broken when the nanostructure is deformed from 2D to 3D. e, f) Calculated vertical displacement (Δd) versus applied stress and voltage respectively for structure with different arc length. l_1 : 4.6 μm ; l_2 : 4.8 μm ; l_3 : 5.2 μm .

2. Results and Discussion

The nano-kirigami array is built on a metal/SiO₂/Si substrate as shown in Figure 1a. For sample preparation, well-designed curves are etched on the metal film, which is just like a paper-cutting process. Then selective wet etching of SiO₂ is applied to obtain a suspended 2D nano-kirigami structure so that there is sufficient space for subsequent deformation. The prepared 2D planar structure can be “folded” in two directions, that is, upward and downward. The downward deformation mode can be aroused by electronic bias as shown in Figure 1b. Specifically, the reconfiguration scheme starts with an array of 2D metal spirals suspended above SiO₂ pillars. When a proper voltage is applied, an electrostatic force will be introduced between the top suspended nanostructures and the bottom silicon substrate, leading to the redistribution of stress within the nanostructures until a new equilibrium state is reached. Under the joint action of mechanical restoring forces and electrostatic force, reconfigurable nano-kirigami transformations can be easily achieved by switching on and off the voltage.

The upward deformation can be achieved by global irradiation of the ion beam as shown in Figure 1c. The twisting deformation is caused by the topography-guided stress equilibrium between the tensile stress and compressive stress that is induced by sputtering-resulted vacancies and ion implantation, respectively, during global ion beam irradiation.^[23] The significance of such a shape transformation is that when the nanostructure is deformed from 2D to 3D, the mirror symmetry of the structure with respect to the xy plane is broken (Figure 1d). The shape and width of these line slits are changed, resulting in remarkable opti-

cal modulation effects (detail discussion see Note S1, Supporting Information). Moreover, the geometric parameters of the curve will affect the strength distribution and the displacement of the deformation of the structure. Figure 1e, f calculated the deformation height/depth of the same curve with different lengths under two different deformations. It shows that structures with longer curves are easier to deform.

As shown in Figure 1b, c, the 3D deformation of nano-kirigami structures can not only cause changes in resonant absorption/emission intensity but also cause changes in resonant absorption/emission wavelength. These trends are strongly related to the shape, structure parameters, and driving mode of the kirigami structures. In the following two examples, we first design a helical-shaped kirigami structure, that is suitable for electrical modulation and capable of modulating emission intensity. Further, we design a pinwheel-shaped kirigami structure, which can achieve large torsional deformation under stress guidance, and can realize large-range emission wavelength shift. Based on these designs, we can choose suitable nano-kirigami structures and driving modes to meet diverse application requirements.

We first demonstrate the static and dynamic thermal emission characteristics of the planar nano-kirigami structures with helical shapes. For nano-kirigami structures, the geometric design of the structure is particularly important. There are three main parameters for a 2D helical kirigami pattern, that is, the period (p), length (l), and width (w) of the curve slits. By adjusting these parameters, perfect emission of 2D structures can be achieved and tuned in a wide wavelength range. As shown in Figure 2a, the resonant wavelength is redshifted as the period increases. Moreover, larger length, smaller width, and more arms also make the

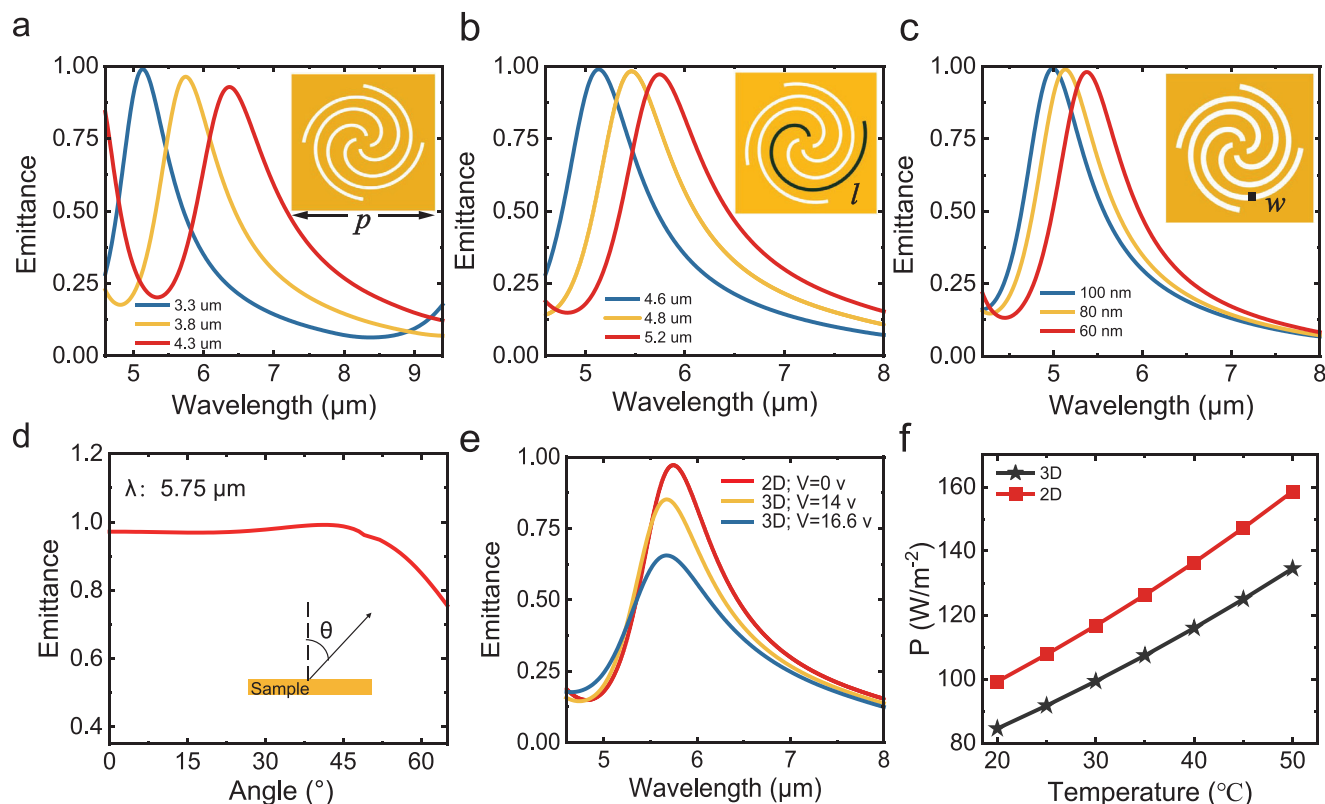


Figure 2. Calculated spectral performance of helical kirigami structures. a–c) Emission spectra of the 2D helical slits with different period a) p , b) arc length l , and c) slit width w . d) Angular dependence of emittance at the resonant wavelength. e) Emittance under different applied voltages. It can be seen that the emission decreases with the increase of voltage. The structure has a parameter of $l = 5.2 \mu\text{m}$, $p = 3.3 \mu\text{m}$, and $w = 80 \text{ nm}$ in the analysis. f) Simulation of the thermal emission power for the 2D (0 V) and 3D (16.6 V) state.

resonant wavelength redshift (Figure 2b,c, and Figure S2, Supporting Information). In comparison, the period is the most sensitive parameter to adjust the emittance. Based on these observations, one can flexibly achieve perfect emission at specific wavelengths. Furthermore, our nano-kirigami structures have an angle-insensitive property. Figure 2d shows that the infrared emission peak of the structure exhibits a distinct angular-independent feature up to 60° . Both the perfect emission and angle insensitivity make our design suitable for a variety of applications such as infrared sensing, thermophotovoltaics, and radiation cooling.

By applying an electric bias between the Au layer and the bottom Si layer, the helical structure will deform downward under the action of electrostatic force, causing the change of emittance and radiation intensity as shown in Figure 2e. With the increase in voltage, the emittance peak of the helical structure decreases with a slight blueshift of wavelength until the maximum voltage (16.6 V) is reached. The existence of the maximum voltage means that the yield strength of the nanostructure and the electrostatic force action reach the maximum equilibrium state. In addition, Figure 2f characterizes the radiated power of the structure at the maximum deformation and the 2D structure at different temperatures. This proves that the device can effectively adjust its infrared imaging effect.

To experimentally demonstrate the dynamic regulation of thermal emission based on electromechanical nano-kirigami, a 2D

nanostructuring process is conducted (Figure 3a). Specifically, a commercial SiO_2/Si substrate coated with a 60 nm-thick Au film was processed with a focused ion beam (FIB) or electron-beam lithography (EBL), accompanied by a wet etching process. As long as the deformable 2D nanopatterns are successfully suspended on SiO_2 supporters, the freely suspended nanostructures can be pulled downward by electrostatic force when a proper voltage is applied, as illustrated in Figure 3b. Figure 3c,d illustrates the variation of reflectance/emittance of the helical structures with different voltages in the visible and mid-infrared wavelengths, respectively. Both show a notable modulation capability of the device. The difference between the experimental and calculated results is due to the structural deviation caused by the wet etching process and the contact resistance in the device (detail discussion see Note S3, Supporting Information).

The nano-kirigami structures can not only dynamically regulate the thermal radiation intensity, but also dynamically control the wavelength range of thermal radiation and the transmission/absorption of visible light, so as to achieve efficient thermal management. To demonstrate this capability, we design a thermal management device based on polymer-mediated 3D nano-kirigami structures with a pinwheel shape (Figure 4). As shown in Figure 4a, the pinwheel kirigami structures can work like a window in the visible wavelengths to reflect or receive solar energy. The linewidth of the 2D structures is much smaller than the wavelength so that it almost reflects all visible light. As the

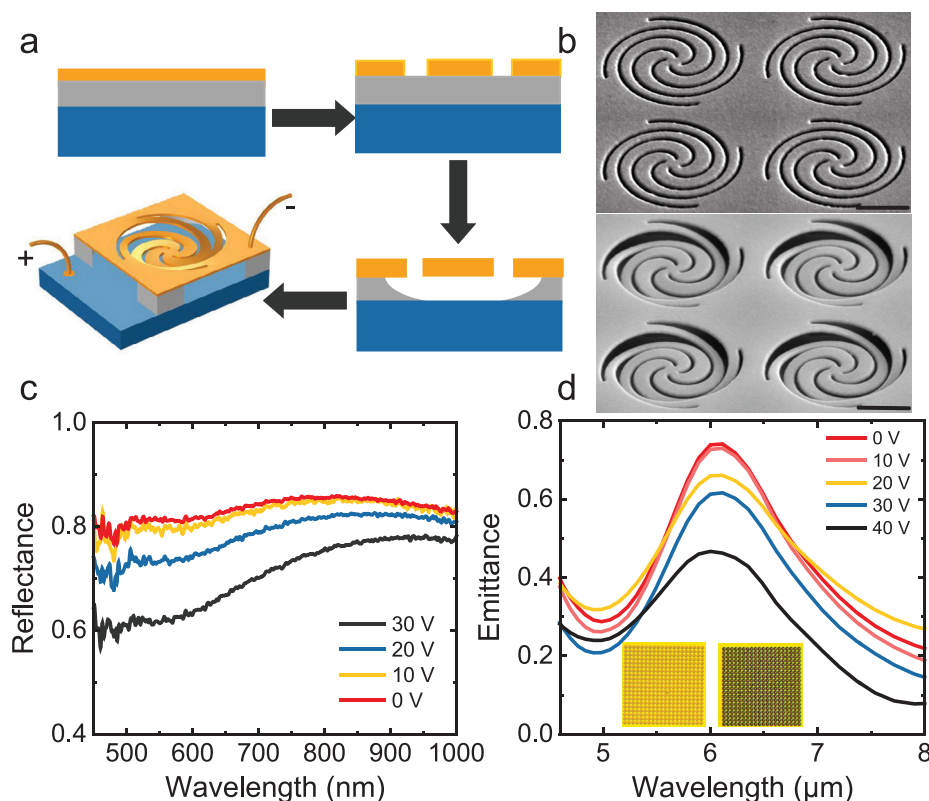


Figure 3. Preparation of the helical kirigami structures and experimental measurement of the dynamic spectrum. a) Fabrication process. Gold: Au; gray: SiO_2 ; blue: Si. b) SEM images of pre-fabricated 2D helical and the downward deformed 3D helical after applying voltage. Scale bars: $1\ \mu\text{m}$. c) Experimental reflection spectra in visible wavelengths under different voltages. d) Experimental emittance spectra in mid-infrared wavelengths under different voltages. The insets show microscope images of the sample under a $20\times$ objective in 0 V (left) and 40 V (right) states. The array size is $65 \times 65\ \mu\text{m}^2$.

deformation height increases, the nano-windows open and the window area continues to increase, resulting in an increase in transmission and absorption (Figure 4b). By combining doped silicon or other absorbing materials at the bottom, the device can effectively control the absorption of solar energy. In the infrared wavelengths, the pinwheel structure can adjust the peak wavelength of thermal radiation. Figure 4c shows the emittance spectrum of silver (Ag) based pinwheel structures with different deformation heights. By carefully designing the structures, we can make the emission peak of the nanostructures located in the wavelength range of the atmospheric window ($8\text{--}13\ \mu\text{m}$) in a 2D state, while the emission wavelength is out of the atmospheric window in a 3D state. So far, many solar absorbers and radiative cooling materials^[28–33] have been reported, but few designs combine the two capabilities and achieve dynamic switching in a thin film structure. Here, we combine nano-kirigami structures with natural solar energy absorption material silicon and natural radiative cooling material PDMS, to achieve the dynamic switching between heating and cooling.

The regulation of cooling and heating is achieved by combining spectral properties of nano-kirigami structures, a doped silicon substrate, and PDMS thin film. The PDMS has two functions here, one is to provide enhanced selective emission in the atmospheric window, and the other is to serve as a stress frame

to drive the deformation of nano-kirigami structure.^[19] Thin film PDMS (thickness $< 20\ \mu\text{m}$) has a selective emittance range in the atmospheric window, but an emission valley at $\approx 10.5\ \mu\text{m}$ which reduces the cooling power (Figure 4d). In order to enhance the cooling performance of the device, the resonance wavelength of the 2D state structure is designed to compensate for the low emittance of PDMS at $10.5\ \mu\text{m}$. Figure 4e illustrates the spectra of our designed device with 3D (black line) and 2D (red line) states in the visible and infrared range against a normalized AM1.5 global solar spectrum (orange shadow) and atmospheric transmittance window (blue shadow), respectively. It shows that the device in a 2D state has almost zero solar energy absorption and highly selective atmospheric window radiation, ensuring a high level of cooling power. In the 3D state, the nano-windows of the device are opened, and transmitted sunlight is absorbed by the bottom silicon substrate, resulting in high solar energy absorption. At the same time, the emission selectivity in the mid-infrared becomes poorer, reducing cooling performance and increasing heating power.

We prepare the thermal management device on a substrate coated with a 60nm-thick Ag film. Three different 2D pinwheel structures are fabricated, and the 3D deformation is realized by using FIB irradiation (Figure 5a–c). The irradiated 3D structure was then coated with a uniform layer of PDMS by spin coating

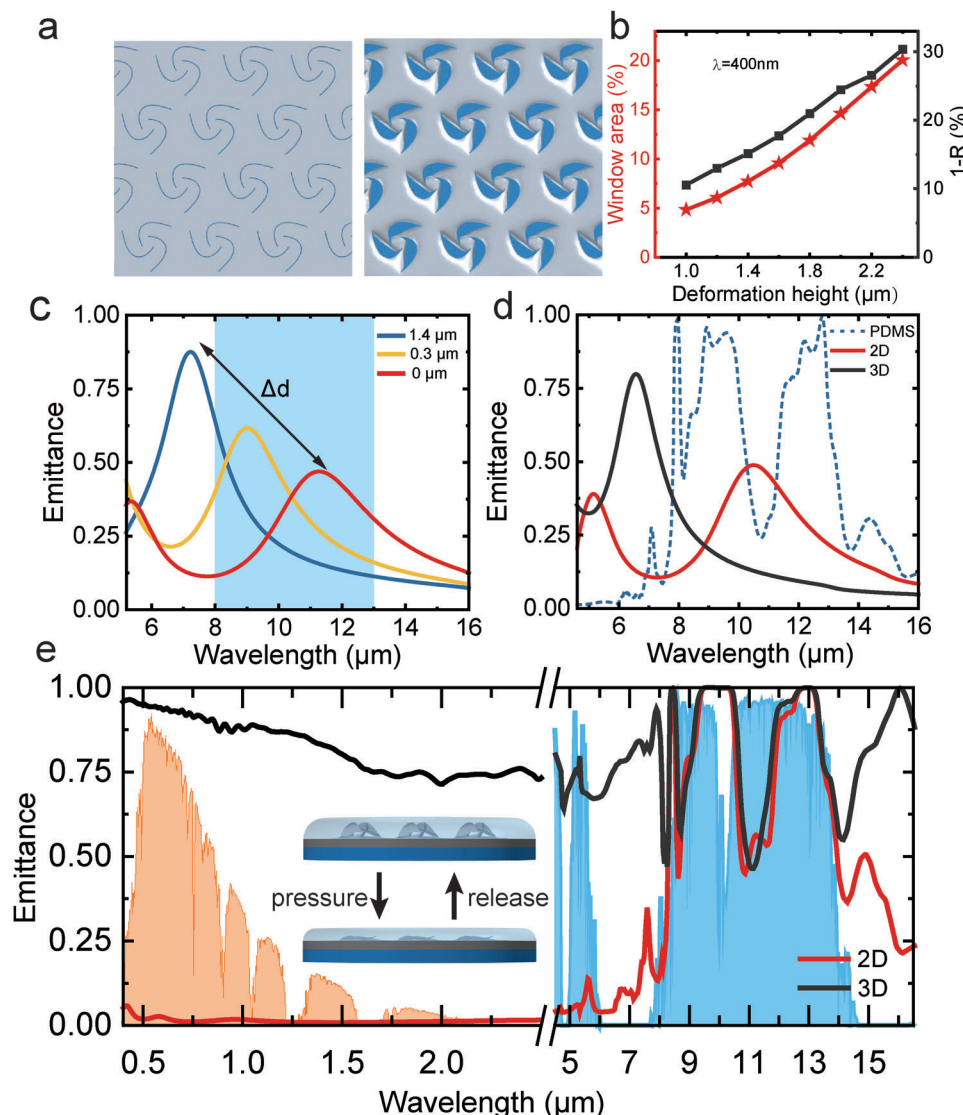


Figure 4. Design of thermal management device based on pinwheel kirigami structures. a) Schematic of the nano-kirigami array before and after deformation in top view. b) Variation of window area and response to visible light with different deformation heights. c) Emittance of the kirigami structures with different deformation heights. Red line: 0 μm; yellow line: 0.3 μm; blue line: 1.4 μm; d) emittance of the kirigami structures in 2D and 3D states. The dashed lines correspond to PDMS with thicknesses of 5 μm. e) Visible and infrared emittance spectra of the pinwheel structures with PDMS framework and silicon substrate in 2D and 3D state. The orange and blue shades are the solar spectral and atmospheric window, respectively.

(3000 rpm, 5 min), which is about 5 μm thick. The 3D nano-kirigami structure could transform back to a flat state with stress from top to bottom. When stress fades, the elasticity of PDMS allows the structure to recover to its initial 3D state. Figure 5d illustrates the emittance of the pinwheel structure with 3, 4, and 6 arms, respectively, in the visible and infrared range, which show consistent spectral change predicted by our calculation. A simpler structure reduces the optical absorption in the visible wavelengths. It can be seen from the comparison of the spectra that the three-arm pinwheel structure has a stronger reflection of visible light in the 2D state and a more obvious change in mid-infrared wavelengths, which means that it can achieve better dynamic thermal management compared to the other two nanostructures.

We further analyze the cooling power (2D) and heating power (3D) of the three-arm pinwheel device according to the spectrum performance (Figure 5e,f), which can be described as follows.

$$P(T_s, T_a) = P_{\text{rad}}(T_s) - P_{\text{atm}}(T_a) - P_{\text{solar}} - P_{\text{cond+conv}} \quad (1)$$

where P_{rad} is the radiated power determined by its surface temperature T_s ; P_{atm} is the power of the atmosphere radiation at temperature T_a ; P_{solar} is the power of solar radiation; $P_{\text{cond+conv}}$ is the direct absorption of heat from the environment through heat conduction and heat convective exchange. When $P(T_s, T_a) = 0$, an equilibrium state is reached between the device and environment, forming a steady-state temperature distribution. We calculate the difference between the stable temperature

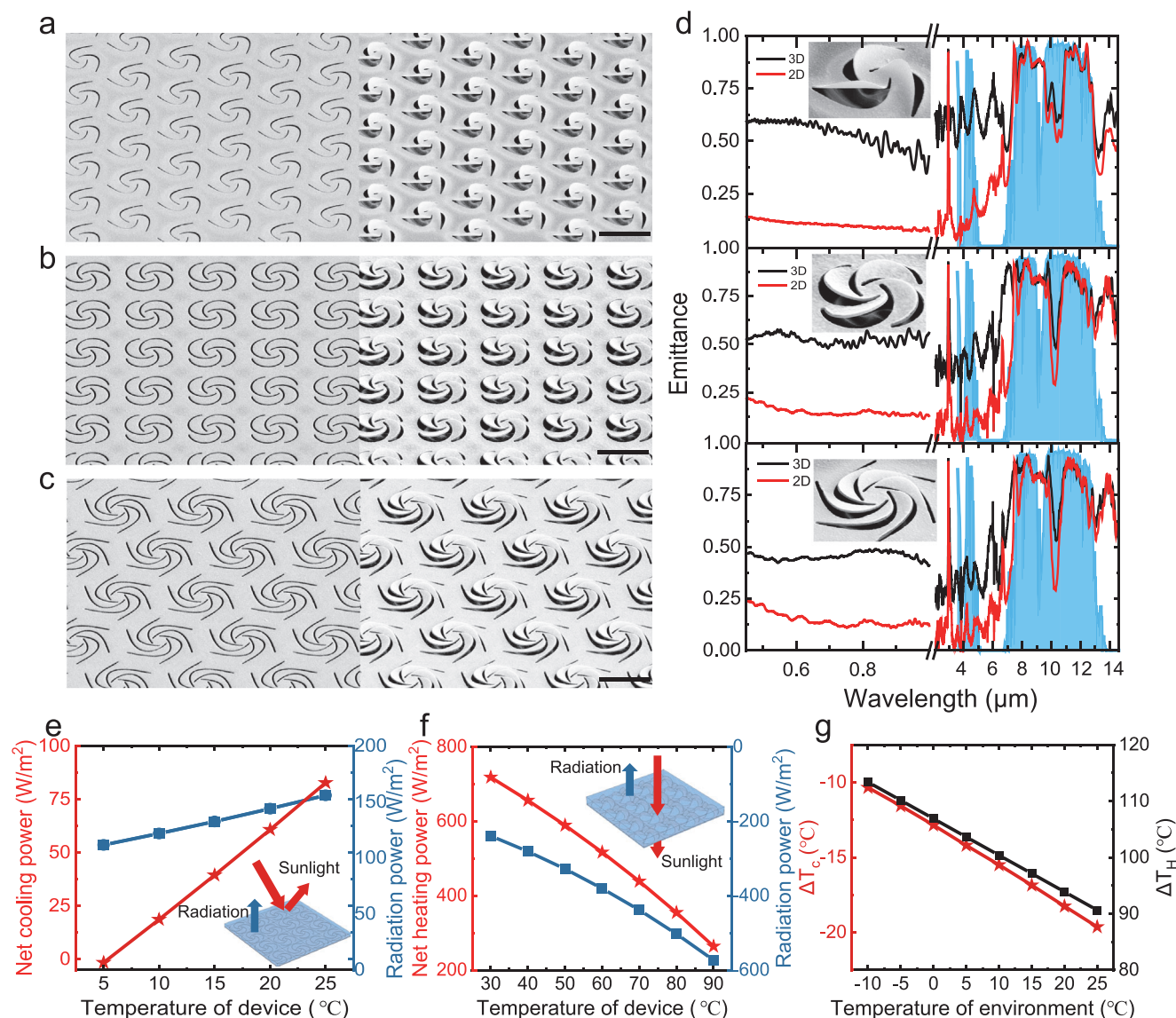


Figure 5. Preparation of the thermal management devices and their optical performance. s, b, c) SEM images of pre-fabricated 2D pinwheels with a) 3 and b) 4 and c) 6 arm, as well as the corresponding upward deformed 3D pinwheels. Scale bars: 5 μm. d) Measured visible and infrared emittance of the pinwheel structures with different arms covered by PDMS in 2D (red line) and 3D (black line) state. The blue shade denotes the atmospheric window. e) Simulated net cooling power of the device at 2D state. f) Simulated net heating power of the device at 3D state. g) Calculated temperature difference between the device and ambient temperature at cooling and heating state.

achieved by the device at different ambient temperatures (Figure 5g). When the ambient temperature is 25 °C, the device can achieve a cooling temperature of about 5 °C and a heating temperature of about 115 °C, which shows an efficient heating and cooling effect.

3. Conclusion

Based on the theoretical analysis and experimental demonstrations presented, our nano-kirigami micromechanical system offers three advantages. Firstly, it enables a multi-physical control method, which allows for dynamic tuning via electrostatic force or mechanical pressure for the same kirigami structure. In ad-

dition, nano-kirigami structures can be manipulated by air pressure, thermal-induced stress, magnetic-induced stress, and other ways.^[27,34,35] As such, we can achieve dynamic regulation of thermal radiation in a convenient way according to the requirements of different application scenarios.

Secondly, it offers multidimensional regulation capabilities, in terms of wavelength, intensity, and other optical properties. Our device has been demonstrated to independently regulate radiation intensity, and can also regulate radiation peak wavelength over a wide range. Because of the elastic changes and 3D spiral structure brought by the special linear design, nano-kirigami structures also have the potential to regulate phase, polarization, and chirality.

Lastly, our nano-kirigami micromechanical system is not restricted to a single material. We have proved that the thermal radiation control of nano-kirigami based on gold and silver in this work. Other plasmonic materials, such as aluminum and magnesium, as well as semiconductor materials such as silicon, and phase change materials such as vanadium oxide, are capable of the preparation of kirigami structures. Therefore, suitable materials can be selected for device design according to needs in multiple application scenarios and environments such as radiation cooling, solar energy utilization, and thermal camouflage.

In summary, we have theoretically designed and experimentally demonstrated a metamaterial thermal emitter for dynamic emission control based on nano-kirigami structures. The helical/pinwheel kirigami structures illustrate the unique ability to regulate the intensity and wavelength of thermal emission. By etching the curves with different parameters onto the metal/SiO₂/Si layer, selective thermal emission is achieved, which can be further tuned by employing electrostatic or mechanical forces. We also demonstrated a thermal management device through the combination of nano-kirigami structures and the PDMS framework. The strong spectral regulation capability and the unique dynamic regulation methods make the proposed nano-kirigami structures an ideal platform for reconfigurable thermal emission while inspiring further development of metasurface for solar energy conversions and radiative cooling.

4. Experimental Section

Numerical Simulations: Mechanical simulations of structural transformations were performed by using the finite element software COMSOL, and the electrostatic interactions between gold film and bottom silicon substrate were simulated to be the actuating force for the structural deformations. An implicit solver was implemented to bypass the numerical singularity around the device's pull-in voltage. As for frequency response, eigenfrequency analysis was conducted on the deformed structures under the applied voltages ranging from zero to the near pull-in voltage. The mechanical transformations of nano-kirigami metamolecules were obtained by adopting a bilayer stress distribution model. The reflection and transmission spectra of both initial 2D patterns and resulting 3D nano-geometries were simulated by using the finite-difference time-domain method. Periodic boundary conditions along the x- and y-axis directions were applied to the unit cell of the simulated structures. The emittance of the structures was equal to the absorptance according to Kirchhoff's law of thermal radiation.

Sample Fabrications: The 2D structures were fabricated with a dual-beam FIB/SEM system (FEI Helios 600i) on a metal/SiO₂/Si substrate. The helical curve was built on the commercial Au/SiO₂/Si substrates (60 nm Au, 300 nm SiO₂). The 2D patterns were directly cut by the FIB under high doses of 1.9×10^8 ions per mm (>600 pC μm^{-2}). The acceleration voltage and current beam of Ga⁺ were set at 30 kV and 80 pA, respectively. After the cutting processes, the sample was dipped into diluted hydrofluoric acid (40%, HF:H₂O = 1:4) to etch off the beneath SiO₂, resulting in locally suspended gold nanopatterns on the top. The fabricated samples were finally attached to the circuit board for electrical tests through wire bonding. For the pinwheel structure used for thermal management devices, commercial SiO₂/Si substrates (500 nm SiO₂) or silicon nitride film windows were first deposited with 5-nm-thick chromium and 60-nm-thick silver. Next, the 2D patterns also followed the etching steps as described above. Subsequently, global ion beam irradiation was conducted by frame-scanning the effective sample area with relatively low doses of 10 to 40 pC μm^{-2} without particular alignment. Finally, the PDMS-mediated

polymer was prepared by mixing Sylgard 527 gel and Sylgard 184 elastomer (Dow Corning) at a weight ratio of 10:1, which was then spin-coated on the top of the sample (5000 rpm, 5 min).

Optical Characterizations: The optical measurements in the visible wavelength range were performed using a home-built spectroscopy system designed to characterize samples with small sizes. For reflection spectral measurement, visible white light from a tungsten halogen source (HL-2000, Ocean Optics) was focused onto the sample by a near-infrared objective lens ($\times 10$, NA 0.25, Olympus). The reflected light in the normal direction was collected by the same objective and delivered to a spectrometer (Ocean Optics, QE65000 for visible wavelengths). For the reconfiguration test, the DC voltage was supplied by a source meter (Keithley 2450). The infrared reflectance of the samples is measured by using an FTIR spectrometer (Bruker vertex 80v) combined with an infrared microscope. The highly doped and sufficiently thick substrate silicon allowed all light incident on the structure to be reflected or absorbed, the emittance (E) was defined by $E(\lambda) = A(\lambda) = 1 - R(\lambda) - T(\lambda)$, where R , T , and λ are the reflectance, transmission, and wavelength, respectively.

Supporting Information

Supporting Information is available from the Wiley Online Library or from the author.

Acknowledgements

Y.Z. and Q.L. contributed equally to this work. This work is supported by the National Natural Science Foundation of China (Grant Nos. 62205022, 61975016, 12274030, 11704075), the Natural Science Foundation of Beijing Municipality (Grant Nos. Z190006 and 1212013), the National Key Research and Development Program of China (Grant No. 2022YFA1403400), and the Beijing Institute of Technology Research Fund Program for Young Scholars. The authors thank the Analysis & Testing Center of Beijing Institute of Technology.

Conflict of Interest

The authors declare no conflict of interest.

Data Availability Statement

The data that support the findings of this study are available from the corresponding author upon reasonable request.

Keywords

dynamic, nano-kirigami, thermal emission, thermal management

Received: June 20, 2023

Revised: August 19, 2023

Published online:

- [1] Y. Zhu, H. Luo, C. Yang, B. Qin, P. Ghosh, S. Kaur, W. Shen, M. Qiu, P. Belov, Q. Li, *Light: Sci. Appl.* **2022**, *11*, 122.
- [2] M. Zhou, H. Song, X. Xu, A. Shahsafi, Y. Qu, Z. Xia, Z. Ma, M. A. Kats, J. Zhu, B. S. Ooi, Q. Gan, Z. Yu, *Proc. Natl. Acad. Sci. USA* **2021**, *118*, 2019292118.
- [3] J. Li, Y. Liang, W. Li, N. Xu, B. Zhu, Z. Wu, X. Wang, S. Fan, M. Wang, J. Zhu, *Sci. Adv.* **2022**, *8*, abj9756.

- [4] S. Wang, T. Jiang, Y. Meng, R. Yang, G. Tan, Y. Long, *Science* **2021**, 374, 1501.
- [5] A. Lenert, D. M. Bierman, Y. Nam, W. R. Chan, I. Celanovic, M. Soljacic, E. N. Wang, *Nat. Nanotechnol.* **2014**, 9, 126.
- [6] L. Dobusch, S. Schuler, V. Perebeinos, T. Mueller, *Adv. Mater.* **2017**, 29, 1701304.
- [7] D. M. Bierman, A. Lenert, W. R. Chan, B. Bhatia, I. Celanovi, M. Soljai, E. N. Wang, *Nat. Energy* **2016**, 1, 16068.
- [8] H. Wei, J. Gu, F. Ren, C. Geng, H. Guan, S. Liang, Q. Fan, J. Zhao, C. Wang, S. Dou, Y. Li, *Laser Photonics Rev.* **2022**, 16, 2200383.
- [9] Z. Xu, H. Luo, H. Zhu, Y. Hong, W. Shen, J. Ding, S. Kaur, P. Ghosh, M. Qiu, Q. Li, *Nano Lett.* **2021**, 21, 5269.
- [10] J. Hildenbrand, C. Peter, F. Lamprecht, A. Kürzinger, F. Naumann, R. Wehrspohn, J. Wöllenstein, *Smart Sensors, Actuators, and MEMS IV. SPIE* **2009**, 7362, 232.
- [11] E. Sakat, L. Wojszwyk, J. P. Hugonin, M. Besbes, J. J. Greffet, *Optica* **2018**, 5, 175.
- [12] T. Mori, Y. Yamauchi, S. Honda, H. Maki, *Nano Lett.* **2014**, 14, 3277.
- [13] T. Inoue, M. De Zoysa, T. Asano, S. Noda, *Nat. Mater.* **2014**, 13, 928.
- [14] C. G. Granqvist, P. C. Lansaker, N. R. Mlyuka, G. A. Niklasson, E. Avendano, *Sol. Energy Mater. Sol. Cells* **2009**, 93, 2032.
- [15] W. J. M. Kort-Kamp, S. Kramadhati, A. K. Azad, M. T. Reiten, D. A. R. Dalvit, *ACS Photonics* **2018**, 5, 4554.
- [16] Y. Qu, Q. Li, K. Du, L. Cai, J. Lu, M. Qiu, *Laser Photonics Rev.* **2017**, 11, 1700091.
- [17] H. Zhu, Hao. Luo, Q. Li, D. Zhao, L. Cai, K. Du, Z. Xu, P. Ghosh, M. Qiu, *Opt. Lett.* **2018**, 43, 5230.
- [18] R. M. Jones, *Mechanics of Composite Materials*, McGraw-Hill, Kogakusha, Tokyo **1975**.
- [19] S. Xiao, T. Wang, T. Liu, C. Zhou, X. Jiang, J. Zhang, *J. Phys. D: Appl. Phys.* **2020**, 53, 503002.
- [20] D. G. Baranov, Y. Xiao, I. A. Nechepurenko, A. Krasnok, A. Alu, M. A. Kats, *Nat. Mater.* **2019**, 18, 920.
- [21] B. Liu, W. Gong, B. Yu, P. Li, S. Shen, *Nano Lett.* **2017**, 17, 666.
- [22] Z. Liu, Y. Xu, C. Y. Ji, S. Chen, X. Li, X. Zhang, Y. Yao, J. Li, *Adv. Mater.* **2020**, 32, 1907077.
- [23] Z. Liu, H. Du, J. Li, L. Lu, Z. Li, N. Fang, *Sci. Adv.* **2018**, 4, aat4436.
- [24] Y. Han, Z. Liu, S. Chen, J. Liu, Y. Wang, J. Li, *Photonics Res.* **2020**, 8, 1511.
- [25] C. Y. Ji, S. Chen, Y. Han, X. Liu, J. Liu, J. Li, Y. Yao, *Nano Lett.* **2021**, 21, 6828.
- [26] S. Chen, Z. Liu, H. Du, C. Tang, J. Li, *Nat. Commun.* **2021**, 12, 1299.
- [27] S. Chen, W. Wei, Z. Liu, X. Liu, S. Feng, H. Guo, J. Li, *Photonics Res.* **2020**, 8, 1177.
- [28] A. P. Raman, M. A. Anoma, L. Zhu, E. Rephaeli, S. Fan, *Nature* **2014**, 515, 540.
- [29] B. Zhu, W. Li, Q. Zhang, D. Li, X. Liu, Y. Wang, N. Xu, Z. Wu, J. Li, X. Li, P. B. Catrysse, W. Xu, S. Fan, J. Zhu, *Nat. Nanotechnol.* **2021**, 16, 1342.
- [30] X. Li, B. Sun, C. Sui, A. Nandi, H. Fang, Y. Peng, G. Tan, P. C. Hsu, *Nat. Commun.* **2020**, 11, 6101.
- [31] T. Li, Y. Zhai, S. He, W. Gan, L. Hu, *Science* **2019**, 364, 760.
- [32] D. Li, X. Liu, W. Li, Z. Lin, B. Zhu, Z. Li, J. Li, B. Li, S. Fan, J. Xie, J. Zhu, *Nat. Nanotechnol.* **2021**, 16, 153.
- [33] J. Mandal, Y. Fu, A. Overvig, M. Jia, K. Sun, N. Shi, H. Zhou, X. Xiao, N. Yu, Y. Yang, *Science* **2018**, 362, 315.
- [34] Y. Chen, Q. Liang, C. Y. Ji, X. Liu, R. Wang, J. Li, *J. Appl. Phys.* **2022**, 131, 233102.
- [35] Y. Zhao, C. Y. Ji, H. Yang, Y. Wang, H. Xie, J. Li, *J. Opt.* **2022**, 24, 054007.